High performance mortars from vitrified bauxite residue; the quest for the optimal chemistry and processing conditions

Peer-reviewed author version

Giels, Michiel; Hertel, Tobias; GIJBELS, Katrijn; SCHROEYERS, Wouter & Pontikes, Yiannis (2022) High performance mortars from vitrified bauxite residue; the quest for the optimal chemistry and processing conditions. In: CEMENT AND CONCRETE RESEARCH, 155.

DOI: 10.1016/j.cemconres.2022.106739
Handle: http://hdl.handle.net/1942/37088

High performance mortars from vitrified bauxite residue; the quest for the optimal chemistry and processing conditions

Journal of Cement and Concrete Research

Giels Michiel[1,*], Hertel Tobias[1], Gijbels Katrijn[2], Schroeyers Wouter[2], Pontikes Yiannis[1]

[1] KU Leuven, Department of Materials Engineering, 3001 Leuven, Belgium

[2] Hasselt University, CMK, Nuclear Technological Centre, Faculty of Engineering Technology, 3590 Diepenbeek, Belgium

*Corresponding author: Giels Michiel: michiel.giels@kuleuven.be

Keywords : bauxite residue, high performance, mortar, cement, concrete.

Highlights:

- Bauxite residue was transformed into a reactive precursor at 1200 - 1300 °C
- Inorganic polymer mortars containing vitrified BR as binder
- Compressive strength up to 130 MPa incorporating 81 wt% bauxite residue
- CaO in the amorphous phase is key to increase strength and reduce shrinkage
- Release of heavy metals and radionuclides below legislative limits

Abstract (max 150 words)

This study investigates the transformation of bauxite residue into a reactive precursor after heat treatment at 1200 – 1300 °C and the synthesis of high performance inorganic polymer mortars thereof. Minor amounts of C, CaO and SiO_2 were added to bauxite residue, and the melt was water-quenched resulting in amorphous phase (25 up to 62 wt%), the rest being mainly iron-rich phases. After milling the vitrified bauxite residue, alkali-activated mortars were produced with a maximum compressive strength of 130 MPa after 28 days. Calcium was identified as key element in increasing the compressive strength, reduction in shrinkage and permeability. The release of heavy metals and

radionuclide concentration were below legislative limits. This work identified an ideal chemistry for producing high-performance binders from precursors containing more than 81 wt% of bauxite residue, opening the possibility of upscaling and, eventually, the real-life transformation of bauxite residue into a product.

1 Introduction

Aluminum is an important metal in today's society due to its light weight, corrosion resistance, thermal behavior and recyclability. The established production process is the Hall–Héroult electrolysis where Al_2O_3, produced typically from bauxite ore via the Bayer process, is smelted. In this process, the ore is dissolved in NaOH under hydrothermal conditions, producing a sodium aluminate solution, which is cooled down to precipitate $Al(OH)_3$ [1]. The remaining fraction, called bauxite residue[1] (BR), or red mud, is thickened, washed and in some plants filter-pressed, to recover most of the remaining alkalis. It is reported that the range of BR generated per 1 ton of Al_2O_3 produced typically varies from 1 to 1.5 tons [2]. This ratio depends on the grade of the ore and the efficiency of the process. With an annual (and increasing) production of 150 Mt of BR, disposal now exceeds 3 billion ton of landfilled BR worldwide [2,3].

For many decades, researchers have been trying to valorize BR using different routes. Many processes have been found to be technically feasible; however, only 2-3 % of the BR is currently used, mainly in the construction industry as Fe and Al source for ordinary Portland cement (OPC)[2] [2]. The latter is also linked to the high volumes of raw materials required by this industrial sector, which often results to a notable valorization of BR.

In construction, concrete and mortars are comprised of a binder, which glues the aggregates together and gives the strength to the material. Here, the use of OPC prevails, which requires only the addition of water for the formation of the binder. However, the production of OPC accounts for 8% of the

[1] BR: Bauxite residue
[2] OPC: Ordinary Portland cement

48 anthropogenic CO_2 emissions [4]. In addition, increasing awareness of the finite natural resources
49 available and the impact of their use has resulted in a growing interest in alternative binders. An
50 interesting group of alternative binders are the group of inorganic polymers[3] (IP), which uses aside
51 water additional alkalis and dissolved silica (e.g., sodium silicate) [5]. One main concern regarding
52 these binders is that often raw materials are used, such as fly ash, blast furnace slag and metakaolin,
53 which are already extensively used in OPC-based systems. Previous studies have indicated the
54 potential of iron-rich calcium-aluminosilicates (i.e., slags from non-ferrous metallurgy) for the
55 synthesis of IP, as these materials are not yet valorised in OPC-based binders [6–10]. Alkali activation
56 allows to produce a F-C-(A)-S-H binder with bivalent iron in trioctahedral phyllosilicates, as well as
57 trivalent Fe in tetrahedral configuration, similar to Al in geopolymers [11,12]. In fact, BR has
58 comparable Fe, Si and Ca content to a non-ferrous metallurgy slags and it would therefore be a good
59 candidate for inorganic polymers.

60 Due to the high fineness, BR has been used in multiple studies as raw material for alkali-activated
61 materials, for instance, in combination with metakaolin, ground granulated blast furnace slag (GGBFS)
62 or fly ash to produce IPs [13]. Increase in viscosity of the mixture, low compressive strengths and
63 sometimes poor durability were reported due to the chemically inert nature of the BR in alkaline
64 media; however, it was also reported that a thermal treatment can increase its reactivity [13–16]. In
65 considering the thermal treatment route, some works focused on transforming Fe depleted BR into a
66 reactive precursor by using an alkali-thermal treatment with temperatures up to 1000 °C [17]. In this
67 process, additional Na_2O was used in order to increase the degree of dissolution of Si and Al. The new
68 precursor, containing peralkaline minerals, C_3A and C_2S, was activated with water, however, poor
69 compressive strength was obtained [17]. This could only be improved by blending other reactive
70 materials to the treated BR [18]. The compressive strength could be increased by the addition of 25

[3] IP: Inorganic Polymer(s)

wt% silica fume to reach a compressive strength of 31.5 MPa for the binder [18]. These findings may have limited impacts due to the high cost of silica fume.

Because treated BR shows low reactivity at temperatures below 1000 °C, it could be transformed to a (partial) amorphous material at higher temperatures (> 1000 °C). This was investigated in the work of [16]. The authors demonstrated that additions of 1.6 wt% carbon (C) and 10 wt% SiO_2 to BR, followed by a heat treatment at 1100 °C, led to partial melt formation, which was transformed into a glass upon quenching [16]. Carbon was an important addition in increasing the amount of glass in the vitrified BR due to the carbothermic reduction of Fe^{3+} to Fe^{2+}. Additional SiO_2 led to an increase in the amount of glass, and a maximum compressive strength of 43 MPa of IP mortars was reached using only the modified BR with a potassium silicate solution. A further study also showed that the reactive precursor could be used to produce porous IP, adsorbing methylene blue [19].

In a later study, the same research group produced three vitrified BRs from bauxite residue, which had different contents of amorphous phase and associated chemistries [20]. It was demonstrated that with a more depolymerized glass structure (amorphous phase structure), a higher reactivity of the precursors was achieved. However, the performance in terms of strength of these binders should be improved in order to compete with currently available conventional binders. The lower processing temperature and lower requirement for natural resources could significantly lower the cost and environmental impact to conventional OPC production. However, a later detailed LCA should assess the process as a whole.

The current work aims to test a bigger range of chemical compositions with additions of C, CaO and SiO_2 in different temperature regions to find the optimal vitrification conditions. Thermodynamic calculations were employed to define an operational window that maximizes the amount of glass, while limiting the vitrification temperature. The effect of crystalline components on the glass is investigated in detail using XRD, (Nano)-SEM and dissolution tests. Furthermore, mechanical performance, shrinkage and permeability of the binders is investigated and linked to each particular

glass chemistry. Finally, the environmental aspects were investigated using end of life leaching tests and naturally occurring radioactive materials due to the presence of radionuclides.

2 Materials and methods

2.1 Characterisation of bauxite residue

BR was delivered in a slurry state by Alum Tulcea (Romania) and was first filtered and dried at 105 ± 5 °C for 48 h. Calcination of the dried BR followed at 950 °C for 8 h, merely for practical reasons so as to be able to fit a larger quantity of the material into the crucible. Thermal analysis was performed on the filtered BR using a TA SDT Q600, measuring the loss of ignition at 1000 °C. Fusion beads for chemical analysis were prepared by fusing a mix of 1.4 g of calcined BR with 12.6 g of lithium borate and lithium bromide at 1050 °C. Chemical analysis of the beads was performed using a Bruker S8 Tiger Wavelength Dispersive X-ray fluorescence spectrometer.

2.2 Processing of the residue

The acquired chemical data and the loss on ignition were used as input for thermodynamic simulations (FactSage 7.0 using FactPS, FToxid and FSstel databases) [21]. The aim of the calculations was to determine the influence of varying additions of CaO and SiO_2 to BR and the effect of temperature (1100 - 1300 °C) on the amount of melt formed. The addition of carbon was considered in all calculations as it has been demonstrated to contribute to an increase in melt formation after carbothermically reducing Fe^{3+} to Fe^{2+} [16]. The calculations aimed to define an operational window in which (i) the amount of melt formed is >50 wt%, so as to achieve a reactive-enough semi-vitrified precursor for IPs after quenching, while (ii) the melting temperature is lower than 1450 °C, so that it is not approaching the conventional cement production.

The different blends were prepared by mixing calcined BR, carbon and varying amounts of SiO_2 and CaO. To obtain a homogenized powder, ethanol and alumina grinding balls (10 mm diameter) were added to the mix and placed in a laboratory shaker (WAB Turbula 2F) for 12 h. After removing the

120 grinding balls, the ethanol was evaporated using a rotary evaporator and additional drying at 80 °C
121 using a laboratory oven.

122 High temperature melting of six BR blends was performed in an induction furnace (Indutherm TF
123 4000). Blends were placed into alumina crucibles, including a lid on top, which were inserted into SiC
124 susceptor crucibles. During heating, N_2 gas was blown on top of the samples at a rate of 60 l/h until
125 1100 °C. At a temperature of 1100-1200 °C, the gas mixture was switched to CO/CO_2 at a rate of 40/20
126 l/h was blown on top to prevent (re)oxidation of the partial melt. After a 2 h period at the target
127 temperature, the melt was quenched in water. Water quenching was shown to be the most suitable
128 method which freezes $FeO\text{-}SiO_2$-rich melts into a glass/amorphous phase [22]. The vitrified bauxite
129 residue (VBR)[4] was subsequently dried at 105 °C, and homogenized and milled in an attritor ball mill
130 1S to a specific surface area of 4400 ± 200 cm^2/g, measured according to EN 196-6.

131 ***2.3 Characterisation of products***

132 The mineralogy of the VBR and of the IP pastes was determined on powder samples by X-ray
133 diffraction (XRD) using a Bruker D2 Phaser X-ray diffractometer. These samples were measured using
134 a CuKα radiation of 30 kV and 10 mA in the range of 5-70° 2 Theta, with a step size of 0.02° and step
135 time of 1 s. For quantification of the mineral phases, powder samples were mixed before the
136 measurements with 10 wt% of ZnO as internal standard and 5 ml of ethanol, and were milled
137 subsequently in a micronizing mill [24].

138 For the investigation of the microstructure of the VBR and IP pastes, samples were embedded in resin,
139 polished and coated with a 1 nm Pt layer and analysed by scanning electron microscopy (SEM)[5] (XL30
140 FEG), operating at 10 kV. Micro-chemical analysis of the VBR was performed using a FEI Nova
141 NanoSEM 450. The chemical composition of the glass and crystalline phases was measured using an

[4] VBR: Vitrified bauxite residue
[5] SEM: Scanning electron microscopy

142 electron beam at 18.5 kV with a spot size of 5 µm so as to obtain a sufficiently high intensity for the
143 measurement.

144 ***2.4 Reactivity***

145 The release of Al, Si and Ca in alkaline solutions was tested as a means to assess the reactivity of the
146 samples. A dissolution test was performed by mixing VBR with a 6M NaOH solution (Milli-Q water
147 based) for 24 h using a solution to VBR mass ratio of 500. The high ratio allows the investigation of the
148 release in far-from-equilibrium conditions to prevent precipitation. The solutions were subsequently
149 diluted 80 times, and the concentration of Si, Al and Ca was measured using ICP-OES (Varian 720ES).
150 Fe was not measured as precipitation was observed in preliminary tests. Other work is now focusing
151 on the complexation of the Fe species, in order to measure the degree of dissolution.

152 ***2.5 Binder production***

153 To prepare the IP pastes and mortars, an activating solution was prepared by dissolving sodium
154 hydroxide pellets (99% NaOH, from Sigma-Aldrich) in a sodium silicate solution (Silmaco, 65% H_2O,
155 SiO_2 25.5–28.5 wt%, Na_2O 7.5– 8.5 wt%). The solution was stored for 24 h at 50 °C to dissolve all the
156 pellets and then cooled to room temperature. IP paste samples were prepared for mineralogical,
157 microstructural and thermal analysis by mixing the activating solution with VBR using a liquid/solid
158 (L/S) ratio of 0.4, which maintained the flow ability of the mixture. 7 day old samples were prepared
159 for thermal analysis by mixing 3 times crushed paste with isopropanol (for 5 min) in order to remove
160 the free water. Samples were vacuum-filtered at each step, then finally mixed with diethyl ether to
161 remove the remaining isopropanol. Samples were degassed afterwards in an oven for 8 min at 40 °C
162 and cooled down in a desiccator. Thermal gravimetric analysis (TA SDT Q600) on these powders was
163 performed using a heating rate of 10 °C/min under a nitrogen atmosphere.

164 ***2.6 Mortar production***

165 IP mortars (3 bars) were produced by mixing the sodium silicate activating solution (SiO_2/Na_2O=2.0,
166 65% H_2O) (220 g) with VBR (550 g) and CEN sand (1350 g). This procedure only deviates from relevant

167 standards [25] in terms of the amount of binder, which is adjusted because of the higher density, and
168 L/S ratio, as previous tests have shown a lower amount of liquid is required for this material. After
169 casting, the samples were cured at 20 ± 2 °C. After 24 h, the samples were demoulded and the prisms
170 wrapped in plastic foil and stored at 20 ± 2 °C.

171 Samples for drying shrinkage were demoulded after 24 h and cured without a cover in ambient
172 conditions (20 ± 2 °C and 40 ± 10 % humidity), while measuring the length change at different time
173 intervals using a dial gauge. The degree of efflorescence (surface carbonation) of the samples without
174 a cover was evaluated visually. Compressive and flexural strength of the wrapped mortar samples
175 were tested using an Instron 5985 testing machine with a load rate of 2 mm/min and 1 mm/min,
176 respectively. An IP based mortar using Koranel® (Metallo), a fully amorphous, non-ferrous slag, was
177 prepared in the same way as the VBR samples and added as reference for comparison.

178 ***2.7 Permeability of mortars***

179 The gas permeability of the samples was determined with a nitrogen permeameter. Plugs of 28 d old
180 samples were first put in isopropanol for 7 d. Afterwards, the plugs were dried further at 80 °C for 24
181 h and mounted in a Hassler type core holder at a confining pressure of 200 psig and a steady state gas
182 flow was established through the sample. The flow rate, pressure differential, gas temperature and
183 ambient pressure were recorded. These parameters were used in conjunction with the callipered
184 length and diameter of the plugs to compute the permeability from Darcy's equation. The
185 permeabilities were corrected for gas-slippage using an empirical Klinkerberg correction.

186 ***2.8 Environmental leaching assessment***

187 The potential mobility of heavy metals was investigated for the different mortars by means of a batch
188 leaching test. The material size was reduced to a particle size <4 mm and leached with deionised water
189 in accordance with EN 12457-4 (2002). This norm is used to assess the environmental safety of the
190 waste in terms of release for a wide spectrum of heavy metals. The leachate was analysed for As, Ba,
191 Cd, Cr, Cu, Mo, Ni, Pb, Se and Zn by an ICP-OES (Varian-720 ES). The acquired data were classified using

192 the directive EC 2003/33/EC [27]. The chosen leaching test simulates the end of life and represents
193 the landfilling leaching limits. It has to be noted that this represents a worst case scenario; recycling
194 of the materials synthesized herein is preferable in view of achieving a circular economy.

195 Another environmental aspect to consider is the presence of naturally occurring radionuclides in
196 building materials, which is regulated by the European Union Basic Safety Standards, wherein the
197 calculation of the activity concentration index (ACI)[6] is prescribed as a screening tool for radionuclide
198 exposure. To ensure compliance with these regulations, one selected mortar sample was evaluated
199 as a case study. The activity concentrations (in Bq/kg) of the naturally occurring radionuclides (NOR)
200 from the decay chains of ^{238}U and ^{232}Th, and ^{40}K were measured using gamma spectroscopy, after
201 storing the crushed mortar sample in a radon-tight polystyrene cylindrical container of 250 cm³ with
202 metal screwcap for 30 d to obtain secular equilibrium between ^{226}Ra and ^{228}Th and their progenies. A
203 detailed description of the detector, experimental set-up and methodology can be found in the work
204 of [28]. Using the obtained activity concentrations of the NOR, the ACI was calculated using Eq. 1, with
205 ^{226}Ra activity concentration expressed as A_{Ra-226} [29].

206 $$ACI = \frac{A_{Ra-226}}{300\ Bq/kg} + \frac{A_{Th-232}}{200\ Bq/kg} + \frac{A_{K-40}}{3000\ Bq/kg} \quad \text{(Eq. 1)}$$

207

208 ## 3 Results and discussion

209 ### *3.1 Characterization of bauxite residue*

210 TGA of BR up till 1000 °C showed a loss of ignition of 11.7 wt%. The chemistry of the dried BR is
211 characterized by a high concentration of Fe, followed by Al and Si (expressed as oxides in Table 1).
212 Minor quantities of Na, Ca and Ti were also present. Hematite, goethite, gibbsite, cancrinite, calcite

[6] ACI: Activity concentration index

and quartz were identified in BR as received and hematite, nepheline and perovskite were the crystalline phases detected after calcination at 950 °C (Fig A1).

Table 1: XRF results of the calcined BR measured on Li-Borate fused beds.

wt%	Fe_2O_3	Al_2O_3	SiO_2	Na_2O	CaO	TiO_2	Other
BR_RO	46	23	13	9	5	3	1

3.2 Thermodynamic calculations and experimental design

For the thermodynamic calculation, the chemistry measured by XRF was used as input (Table 1). Through the addition of C, the Fe^{3+} of BR was transformed into Fe^{2+}, which has been shown to lead to increased melt formation. For the experimental work, the C/Fe_2O_3 was fixed at 0.05; initial calculations showed that by increasing this ratio the formation of metallic iron, and thus a reduction in melt quantity, was predicted. Because the material in the crucible is not completely protected from interaction with surrounding air, in the final calculation a pO_2 of 10^{-9} atm is assumed in the thermodynamic calculations, as shown in the work of [20]. SiO_2 was added to increase the amount of melt and CaO was used for depolymerisation of the melt and final amorphous, increasing the reactivity in alkaline conditions [30,31]. Both fluxes are relatively abundant and easily accessible in the form of sand and limestone. Calculations were performed at 1100, 1200 and 1300 °C, whit a maximum of 20 wt.% additions for SiO_2 and CaO (Figure 1). Results show that an operational window for experiments is defined between 1200 °C and 1300 °C, because more than 50 wt% melt is produced. The amount is already sufficient as it has been shown to already gave adequate performance in IP [16]. In this operational window, a series of experiments was designed with the main focus on the processing temperature of 1200 °C (Table 2). The name number after the element, the amount of the oxide in g, that was added to 100 g of dried BR.

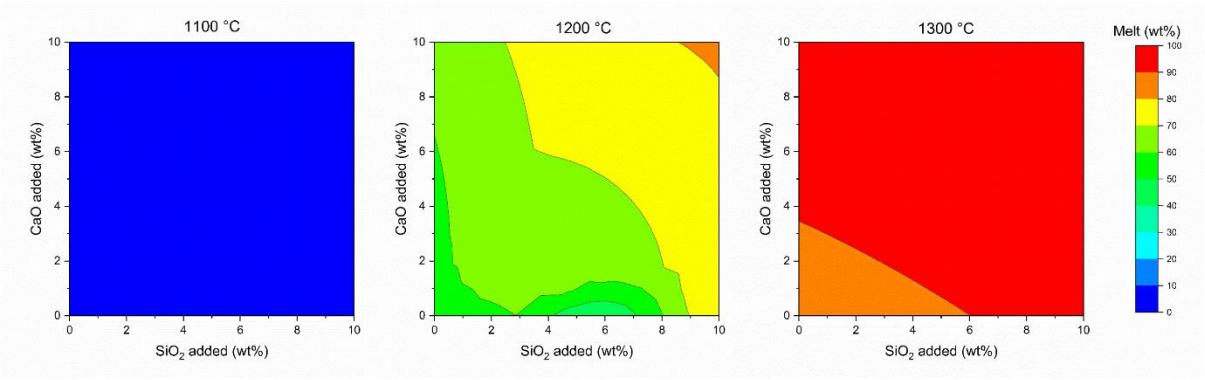

234

235 *Figure 1: Calculated amount of melt at different temperatures using FactSage with a pO_2 of 10^{-9}.*

236

237 *Table 2: The designed mixes for the high temperature experiments.*

Sample	Temperature (°C)	BR (g)	C (g)	SiO_2 (g)	CaO (g)
Si0Ca0-1200	1200	100	2.3	0	0
Si0Ca10-1200	1200	100	2.3	0	10
Si10Ca0-1200	1200	100	2.3	10	0
Si5Ca5-1200	1200	100	2.3	5	5
Si10Ca10-1200	1200	100	2.3	10	10
Si10Ca10-1300	1300	100	2.3	10	10

238

239 ***3.3 Characterization of vitrified bauxite residue***

240 Table 3 show the chemistry of the various mixes after melting and quenching. The Na_2O content
241 remains quite high, which indicates that there was limited volatilization of Na_2O to Na at high
242 temperature. Table 4 shows the quantified mineralogical composition of the different quenched
243 samples (VBR). The diffraction patterns can be found in Figure A2A. Table 4 shows that the amorphous
244 content varies between 28 and 67 wt%. It is also apparent that iron is mainly present in iron-rich
245 phases as (titano)magnetite-hercynite ($Fe(Fe, Al, Ti)_2O_4$), wüstite (FeO) and metallic iron (Fe). Closer
246 inspection also reveals that Si0Ca0, Si0Ca10 and Si10Ca0-1200 contain in addition to these iron-rich
247 phases, some aluminosilicate minerals, such as gehlenite ($Ca_2Al_2SiO_7$) and sodium aluminosilicates
248 phases (e.g. nepheline ($NaAlSiO_4$)). There is a slight difference between calculated (FactSage) and
249 experimental amounts of amorphous phase (Table 4). The reasons for this difference were discussed
250 in [16,20]. The spinel group is quantified using the stoichiometric end-members of the solid solution.

This is justified by the SEM-EDX data in Table 6, showing that a solid solution exists between these end-members.

Table 3: Chemical composition by XRF on Lithium-borate fused beads in wt%.

	FeO	Al_2O_3	SiO_2	Na_2O	CaO	TiO_2	Other
Si0Ca0-1200	43.1	23.3	14.1	9.2	5.2	3.6	1.5
Si0Ca10-1200	38.9	21.0	12.7	8.6	14.1	3.3	1.5
Si10Ca0-1200	39.5	21.1	22.0	8.3	4.8	3.4	1.0
Si5Ca5-1200	39.4	21.0	17.6	8.3	9.3	3.4	1.1
Si10Ca10-1200	35.6	19.7	20.1	7.7	12.9	3.0	1.0
Si10Ca10-1300	35.2	20.1	19.8	7.8	12.8	3.0	1.3

Table 4: Quantitative mineralogical composition of the VBR using the Rietveld algorithm in wt% with standard deviation.

	Si0CaO-1200	Si0Ca10-1200	Si10Ca0-1200	Si5Ca5-1200	Si10Ca10-1200	Si10Ca10-1300
Amorphous	25 ± 5	51 ± 5	45 ± 5	47 ± 6	62 ± 1	62 ± 4
Wüstite	14 ± 1	28 ± 2	9 ± 1	13 ± 2	15 ± 2	27 ± 3
Magnetite	9 ± 1	0 ± 0	11 ± 0	9 ± 2	4 ± 1	3 ± 0
Hercynite	26 ± 2	8 ± 1	26 ± 3	27 ± 2	18 ± 1	8 ± 1
Gehlenite	0 ± 0	6 ± 2	0 ± 0	0 ± 0	0 ± 0	0 ± 0
Nepehline	0 ± 0	0 ± 0	8 ± 1	0 ± 0	0 ± 0	0 ± 0
Sodium alumino silicate	18 ± 1	4 ± 0	0 ± 0	3 ± 1	0 ± 0	0 ± 0
Iron	1 ± 0	0 ± 0	1 ± 0	1 ± 0	1 ± 0	0 ± 0
Titanomagnetite	4 ± 4	0 ± 0	0 ± 0	0 ± 0	0 ± 0	0 ± 0
Ulvöspinel	2 ± 0	3 ± 1	0 ± 0	0 ± 0	0 ± 0	0 ± 0

Figure 2 shows the microstructure of the synthesized VBR under the SEM. The images show that the crystalline phases are embedded in an amorphous matrix. The crystalline phases magnetite-hercynite and iron had an average size of 10 µm in cross-section, whereas the wüstite crystals are micro- to nanometer sized. The wüstite showed a dendritic morphology and grew on the magnetite-hercynite crystals. The (titano)magnetite-hercynite crystals grew on the iron particles, which suggests initial formation of iron followed by spinel and, later, wüstite crystallization. The latter phase(s) could be formed during cooling.

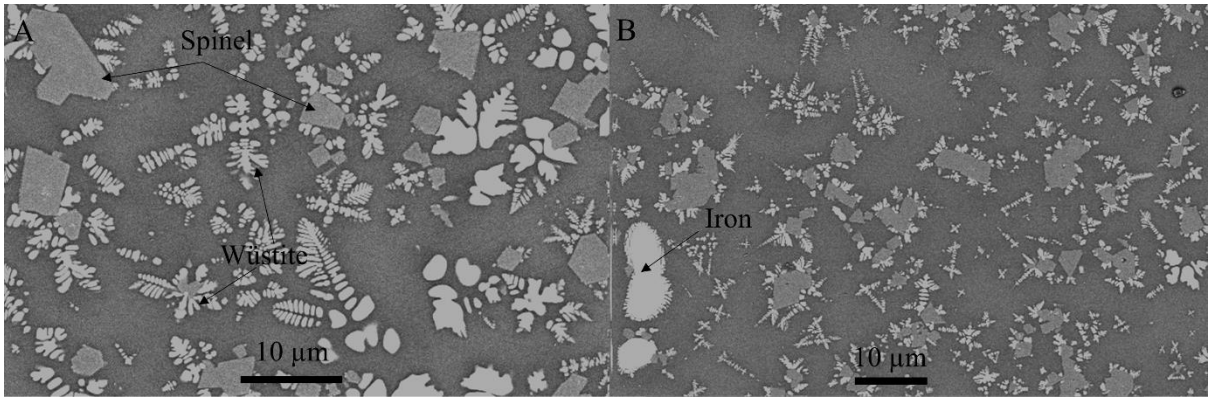

Figure 2: Backscattered electron images of Si0Ca10-1200 (A) and Si10Ca10-1200 (B). Both pictures show the grey glassy matrix containing the iron rich crystalline phases.

Table 5 shows the chemistry of the amorphous phase, which determines the reactivity of VBR. Elements aside the one's mentioned were not detected. The analysis shows that the FeO content is much higher than expected (up to 15 %) when Table 3Table 1, Table 4 and Table 5 are compared. The appearance of Fe-rich phases would lead to a more Fe-depleted amorphous phase. However the higher FeO content is an artifact and probably related to the interaction volume and contribution of identified nano-crystalline phases (Figure A3), which make the amorphous phase difficult to measure. This effect also explains the high standard deviation for FeO. Local heterogeneity in the samples is also likely to influence the measured compositions. Furthermore, the data shows that Si, Ca and Na are increased in glass compared to the bulk composition by a factor of up to 2, which is mainly dependent on the amount of amorphous phase and presence of calcium/sodium alumino silicate phases. The elements Al and Ti are present both in spinel and glass phases.

Table 5: EDX analysis of the amorphous phase in wt% with standard deviation. Due to the interaction of nano-crystaline iron phases a higher amount of FeO is measured than available in the amorphous phase.

	Na_2O	Al_2O_3	SiO_2	CaO	TiO_2	FeO
Si0Ca0-1200	14.9 ± 1.8	21.4 ± 0.7	25.8 ± 1.6	11.4 ± 1.5	3.7 ± 0.6	22.8 ± 3.2
Si0Ca10-1200	10.6 ± 1.3	23.7 ± 2.7	13.9 ± 1.8	18.1 ± 2.9	3.7 ± 0.5	29.9 ± 8.7
Si10Ca0-1200	12 ± 0.9	17.9 ± 1.8	32.8 ± 4.8	7.5 ± 2.2	3.7 ± 7.2	26.1 ± 7.0
Si5Ca5-1200	13.9 ± 1.3	20.1 ± 1.5	27.7 ± 2.5	17 ± 2.2	3.2 ± 0.8	18.0 ± 5.8
Si10Ca10-1200	10.6 ± 1.3	18.2 ± 1.2	25.4 ± 3.0	18.6 ± 3.1	3.1 ± 0.8	24.1 ± 7.2
Si10Ca10-1300	8.7 ± 0.7	21.6 ± 2.8	22.4 ± 2.5	16.9 ± 2.5	3.5 ± 0.5	26.8 ± 7.3

281 Compositional data of the main spinel phase are shown in Table 6. It should be noted that only the
282 larger spinel phases could be measured due to the limitations in the interaction volume of the electron
283 beam. The data show a high standard deviation in the amount of Al_2O_3 and FeO due to the existence
284 of a solid solution between (titano)magnetite and hercynite. The uptake of Mg, Cr and V is more
285 interesting: Cr is most likely present as Cr^{3+} due to the reducing processing conditions. Due to chemical
286 stability of the spinels in the alkaline solution, the Cr is immobilized in its crystalline lattice [20,32].

287

Table 6: EDX analysis of the spinel-phases in wt% with standard deviation.

	Al_2O_3	TiO_2	FeO	MgO	Cr_2O_3	V_2O_5
Si0Ca0-1200	38.7	3.1	58.1	-	-	-
Si0Ca10-1200	53.5 ± 8	1.7 ± 1.5	34.7 ± 7.8	1.6 ± 0.4	2.2 ± 1.8	-
Si10Ca0-1200	45.8 ± 8	4.1 ± 1	48.7 ± 7.3	-	0.5 ± 0.4	0.2 ± 0
Si5Ca5-1200	49.0 ± 9	3.4 ± 0.8	45.7 ± 10.1	-	0.4 ± 0.6	-
Si10Ca10-1200	50.5 ± 12	3.2 ± 0.7	41.3 ± 14.2	0.1 ± 0.3	1.6 ± 1	-
Si10Ca10-1300	52.6 ± 11.9	1.9 ± 0.9	40.6 ± 10.5	0.9 ± 0.4	4.4 ± 1.4	-

The EDX analysis of sodium and calcium aluminosilicate phases which are present in a minor quantity in sample Si0Ca0, Si10Ca0, Si0Ca10 can be found in the appendix (Table A2 & Table A1). These sodium aluminosilicate phases in the samples show a consistent chemistry between the different analyzed particles for each sample; however, there is some variation between the different samples both in of chemistry and crystal structure. Whereas in Si10Ca0 these phases correspond to a nepheline composition with hexagonal crystal structure, the other phases in Si0Ca0, Si0Ca10 and Si5Ca5 have an orthorhombic crystal structure, according to XRD.

For further analysis, the glass chemistry can be converted using the EDX and quantitative XRD data to calculate the amount of reactive mol of a component x for 1 kg of VBR (Eq. 2 and 3). This calculation identifies whether certain elements in the glass phase influence the macroscopic properties, while taking into account the amount and chemical composition of the amorphous phase. Table 7 shows the calculated reactive mol/kg VBR respectively for the different oxides. Fe, Al and Ti are not included due to the higher uncertainty caused by the participation in complex solid solutions. However, because of the significant interaction with the iron-rich nano-crystals, the result of Eq. 3 is most likely more reliable, whereas Eq. 2 will result in an underestimation (Table 7). The results of Eq. 3 are therefore used as predictive variable in this work.

$$Reactive\ mol\ \frac{X}{kg\ TBR} = 10 * \frac{[Amorphous]_{xrd} * [X]_{EDX}}{\text{Molar mass X}} \qquad \text{(Eq. 2)}$$

$$Reactive\ mol\frac{X}{kg\ TBR} = 10 * \frac{[X]_{xrf} - \sum_{i}^{n}([X\ phase]_{qxrd})}{\text{Molar mass X}} \quad \text{(Eq. 3)}$$

Table 7: Calculated reactive mol of SiO_2, Na_2O and CaO/kg VBR using Eq. 2 and 3. Standard deviation based on 3 quantitative XRD samples.

	Reactive mol Na_2O/kg VBR		Reactive mol CaO/kg VBR		Reactive mol SiO_2/kg VBR	
	Eq. 2	Eq. 3	Eq. 2	Eq. 3	Eq. 2	Eq. 3
Si0Ca0-1200	0.6 ± 0.1	1.2 ± 0.4	0.5 ± 0.1	0.7 ± 0	1.1 ± 0.2	2.1 ± 0.5
Si0Ca10-1200	0.8 ± 0.1	1.2 ± 0	1.6 ± 0.1	1.8 ± 0.2	1.1 ± 0.1	1.8 ± 0.1
Si10Ca0-1200	0.9 ± 0.1	1.1 ± 0	0.6 ± 0.1	0.8 ± 0	2.4 ± 0.3	3.1 ± 0.1
Si5Ca5-1200	1.0 ± 0.1	1.2 ± 0	1.4 ± 0.2	1.6 ± 0	2.1 ± 0.3	2.7 ± 0.1
Si10Ca10-1200	1.1 ± 0	1.2 ± 0	2.1 ± 0	2.3 ± 0	2.6 ± 0.1	3.3 ± 0
Si10Ca10-1300	0.9 ± 0.1	1.3 ± 0	1.9 ± 0.1	2.3 ± 0	2.3 ± 0.2	3.3 ± 0

3.4 Reactivity

The different VBR were tested in terms of reactivity by mixing the samples with 6M NaOH (Figure 3). Si and Al are released in high concentrations; however, Ca shows a release below <0.2 wt%. The low release of Ca can be related to precipitation on the surface of the particles [33]. Interestingly, the release of Al was found to be higher than Si, although Al is incorporated in both glass and spinel. This is related to the weaker Al-O-Si bonds compared to Si-O-Si bonds [34]. The released Si was also found to plateau at 30-36 % of the original concentration, which could be related to slower glass dissolution by $H_2SiO_4^{2-}$ adsorption, increased activity of OH^- leading to a decrease of water to fully hydrolyse ionic species and/or precipitation of a hydrated phase on the surface of the particles [33][35]. The release of Al is also significantly higher for Si10Ca10-1300 compared to Si10Ca10-1200, which is most likely related to the higher Al content of the glass. The decrease of the spinel end member Hercynite ($FeAl_2O_4$) Si10Ca10-1300 increases the Al content of the amorphous phase.

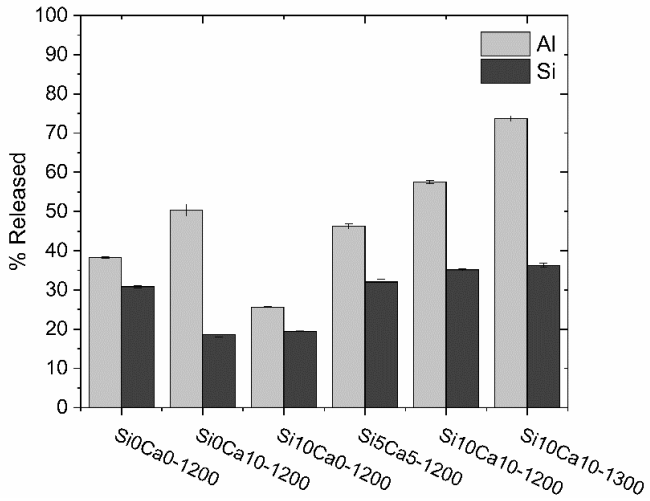

Figure 3: Release of Al and Si in 6M NaOH for 24h.

3.5 Characterization of the binder

The XRD diffractograms, which can be found in the appendix (Figure A2B), showed no new detectable phases after alkali activation in the binder at 28 d; only the crystalline phases of the precursors were detected. The calcium/sodium alumina silicate phase does not show any noticeable dissolution either. The impact is most likely low, because the latter phases are only present in minor amounts. Microstructural investigation of the paste samples in Figure 4 shows that the amorphous phase (glass) dissolved and precipitated a dark grey binding matrix, leaving the mineral phases unaffected. The binder therefore represents the chemistry of the glass with additional Si, Na and H_2O from the activating solution. Thus, the binder can be classified as a N-(F,C)-A-S-H gel. Figure 4 shows the binder that consists of crystals and undissolved particles. These remaining crystals can act as nucleation seeds, affect particle packing and increase space for reaction products due to the so called 'filler effect', which improves the structural properties of the binder [36].

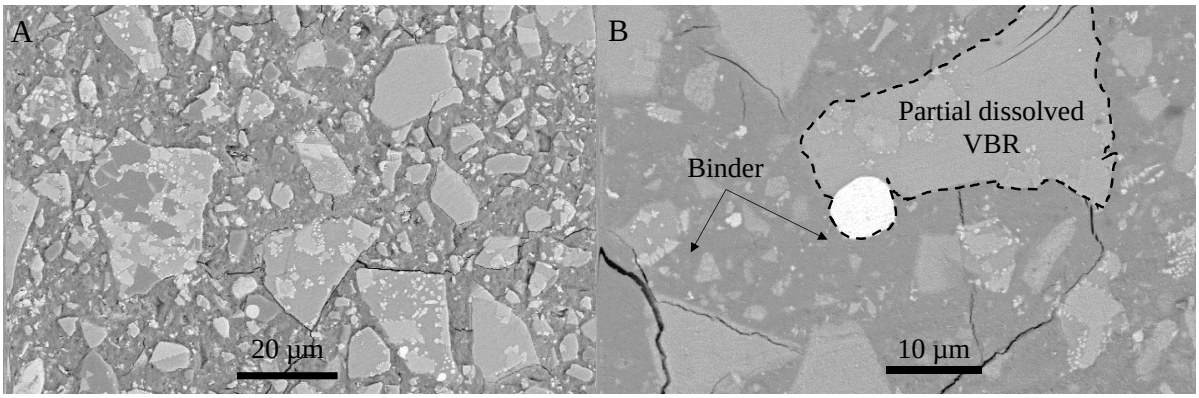

Figure 4: Backscattered electron images of sample IP-Si10Ca0 (A) and IP-Si10Ca10 (B). A) shows the undissolved particles in a binding matrix; B) illustrates the inert nature of the crystalline phases and selective dissolution of the glass.

3.6 Properties of the mortar

The compressive strength of the IPs ranges from 32 to 110 MPa after 7 days and 62 to 131 MPa after 28 d (Table 8). What stands out is the significantly higher 7 and 28 d flexural and compressive strength for samples with CaO additions compared to both the IPs from BR without Ca and the fully amorphous (FeO-Al_2O_3-SiO_2) non-ferrous slag Koranel® with the same mix design. A maximum compressive strength of 110 MPa at 7 d was obtained for samples IP-Si10Ca10-1200 and IP-Si10Ca10-1300. Although IP-Si0Ca10-1200 achieved a compressive strength at 7 d of 98 MPa, it is probably not suitable in an IP system as the setting time was around 10 min. A 28 d compressive strength of 130 MPa was eventually reached for IPSi10Ca10-1300. The late compressive strength increased with respect to IP-Si10Ca10-1200, due to a higher processing temperature, although the amount of amorphous phase and bulk chemistry were similar (Table 5). However, the glass chemistry reveals an increase in Al_2O_3 in the glass at 1300 °C, due to a lower amount of spinel. In addition, reactivity data also shows an increased Al-release for IP-Si10Ca10-1300. This data suggests that Al_2O_3 could be important in increasing the 28 d compressive strength, increasing the amount of binder and the alumina in the gel. A positive impact of Al is also observed in C-A-S-H gels, where Al enhances the chain length of the dreierketten structure, which in turn increases the resistance to compression [37].

Table 8: Compressive and flexural strength of mortars produced from VBR. Standard deviation of the compressive strength testing is based on the testing of 2 samples. One bar was used for determination of the flexural strength.

	7 days		28 days	
	Compressive strength (MPa)	Flexural strength (MPa)	Compressive strength (MPa)	Flexural strength (MPa)
IP-Si0CaO-1200	41.9 ± 0.8	4.0	62.3 ± 0.5	7.3
IP-Si0Ca10-1200	98.6 ± 2.0	11.7	109.2 ± 0.3	13.0
IP-Si10Ca0-1200	32.6 ± 2.4	4.7	81.8 ± 1.7	11.1
IP-Si5Ca5-1200	90.2 ± 2.7	10.5	104.4 ± 1.6	11.6
IP-Si10Ca10-1200	110.8 ± 1.0	11.4	119.6 ± 0.9	14.0
IP-Si10Ca10-1300	110.8 ± 0.3	13.3	131.1 ± 3.6	13.2
IP-Koranel®	59.9 ± 3.4	5.6	72.1 ± 0.5	-

If the reactive amount of each element (Eq 3.) is plotted to compressive strength, only a strong linear correlation between CaO and compressive strength is observed in Figure 5. A similar trend was observed for fly ash based IP [38]. This could be due to 1) Increased dissolution rate and 2) a stronger binder. It is known that the dissolution of glasses in high pH solutions increases with the increasing number of non-bridging oxygen (NBO)[7] to oxygen atoms in tetragonal coordination (T) [39,40]. Calcium atoms increase the amount of NBO, resulting in a higher dissolution rate of the glasses, which translates into higher performance [31]. Aside dissolution speed, increasing the amount of CaO in the IP mix design also leads to higher compressive strength [41]. Research on C-A-S-H gels showed that the increase in Ca and interlayer water make the gels more resistant to compression [37]. However, as discussed above an increased reactive amount of Al_2O_3 also contributes the 28d compressive strength.

[7] NBO: Non-bridging oxygens

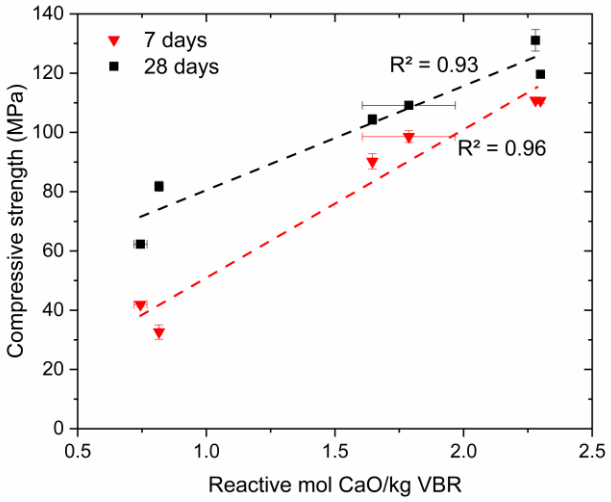

374

375 *Figure 5: Linear correlation of amount of reactive mol CaO/kg VBR with 7d (triangles) and 28d compressive strength (cubes).*

376 Figure 6 shows that the mortar bars shrink when they are in a dry environment due to water loss. The
377 samples shrunk mainly within the first 7 days, which coincided with the biggest water loss. However,
378 a significant weight increase is observed for IP-Si0Ca0 and IP-Si10Ca0 after 28 d. This is linked to the
379 onset of visual efflorescence, incorporating CO_2 from the surrounding environment. This indicates that
380 for these samples, alkalis are not sufficiently bound, which could be due to the lower reaction degree
381 of the VBR in these samples [42]. However, the efflorescence did not affect the dimensional changes
382 of the samples and occurred after the samples stopped shrinking due to water loss. Furthermore, the
383 results show that samples with additional CaO shrunk to a lesser degree than the samples without
384 additional CaO, with deformation as low as -1.5 mm/m after 180 d. This low dry shrinkage is close to
385 the minimal deformation of -0.7 mm/m after heat curing at 100 °C for iron-rich IP [43].

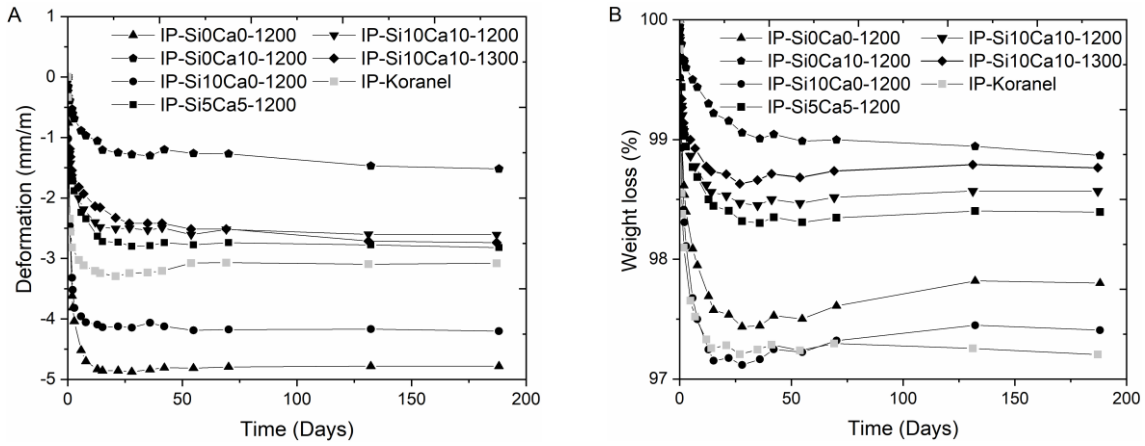

Figure 6: Dimensional change (A) and weight loss (B) of the mortar bars measured over a period of 180 days.

TGA was performed on solvent-exchanged 7 d-old pastes (Figure 7A). In this work the solvent exchange allowed the pore water to be removed. The bound water is, therefore, considered up to 600 °C, before calcite decomposition, which reflects mainly the interstitial and hydroxyl water [44,45].

Figure 7B shows an increased amount of bound water for samples when CaO is added. Moreover, the DTG curve shows that no portlandite is formed, which should start to decompose approximately at a temperature of 460 °C [45]. At temperatures above 650 °C some minor carbonating phases decompose. Figure 7B suggests that the amount of CaO in the glass determines the final bound water content in the IPs and in turn limits deformation during drying. These binders are Ca rich, resulting in a more voluminous binder due to water uptake, which is either stronger and/or has a refined pore structure.

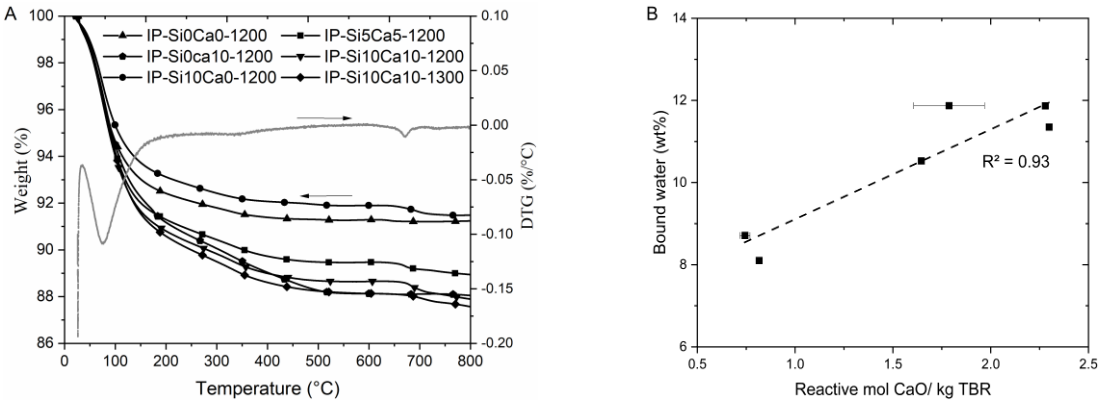

Figure 7: A) Thermal gravimetric analysis (TGA) and differential thermogravimetric analysis (DTG) of the paste samples after solvent exchange. Only 1 DTG is shown representatively due to the high similarity of the curves. B) Plot of bound water versus the amount of reactive mol CaO/kg of VBR.

3.7 Permeability

Table 9 shows that air permeability decreases with increasing the amount of both SiO_2 and CaO. Permeability is for IP-Si10Ca10-1200 and IP-Si10Ca10-1300 half as much as the mortar samples using non-ferrous slag (Koranel). This indicates that the developed mortars with BR treated with a high amount of CaO and some additional SiO_2 result in a denser binder. Permeability of the material is of great importance as this will determine the rate by which species can enter the sample. The lower permeability will most likely for IP-Si10Ca10-1200 & 1300 will result in a significantly increased durability in different (aggressive) environments.

Table 9: Air permeability without and with an empirical Klinkenberg correction for gas slippage.

	IPSi0Ca0-1200	IPSi0Ca10-1200	IPSi10Ca0-1200	IPSi5Ca5-1200	IPSi10Ca10-1200	IPSi10Ca10-1300	IP Koranel®
Gas permebality (mD)	2.23	-	0.34	0.28	0.21	0.19	0.44
Emp. Klink Perm (mD)	1.61	-	0.22	0.18	0.14	0.12	0.29

3.8 Environmental assessment

Figure 8 shows the leaching data from the ground mortars that were cured for 90 d. All mortar types are classified as inert/non-hazardous waste according to EC 2003/33/EC. The data verifies the safe encapsulation of Cr in the spinel phases, however, Se release is elevated and exceeds the limit for non-hazardous waste, for all mortars. IP-Si10Ca10-1200 and IP-Si10Ca10-1300 show heavy metal leaching under the limit, except for Se. This increase can be linked to its anionic nature, which resides in the pore solution due to its pH dependence. If the binder carbonates, the release of oxyanions will likely be decreased [46]. Leaching could also be influenced to dilution through the addition of additives. However, this effect seems to be only of minor importance as difference in release varies between up to 80%. Most likely a combined effect of mineralogy and microstructure is influencing the release. Overall, the best performing mortars IP-Si10Ca10-1200 and IP-Si10Ca10-1300 are considered to be non-hazardous.

For IP-Si10Ca10-1200 the activity of different radionuclides was measured. The earth's crust contains on average activity concentrations of 40 Bq/kg for ^{226}Ra and ^{232}Th and 400 Bq/kg for ^{40}K [47]. The

obtained activity concentrations for the respective NOR in the IP mortar sample are significantly lower (Figure 8B). This is presumably due to the diluting effect caused by the standard sand and the additions of 19 wt% fluxes, which likely contains negligible natural occurring radioactivity concentrations. However, it has been reported that most of the BR contains low concentrations of natural occurring radioactivity [48,49][50][51]. The calculated ACI gives a value of 0.0690 ± 0.0057, which is well below the screening value of 1. This means that the IP mortar can be used for indoor applications without legislative constraints from a radiological protection point of view [29][28].

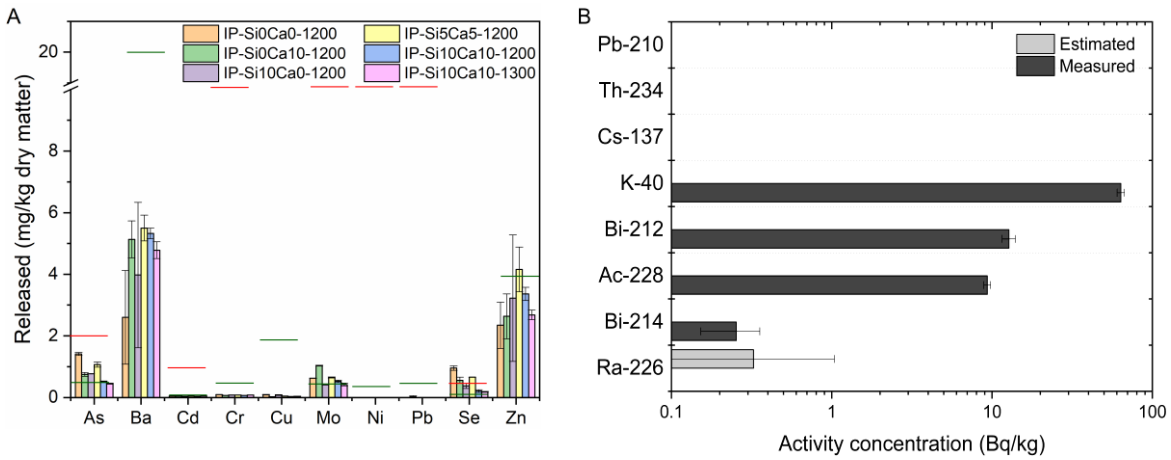

Figure 8: A) Leached concentrations of heavy metals in mg/kg dry matter with standard deviation. The limit for inert waste is visualised with a green bar and for non-hazardous waste with a red bar. B) Activity concentrations for sample IP-Si10Ca10-1200 in Bq/kg.

4 Conclusion

This study explored and confirmed the technical feasibility of producing high performance binders from VBR. Processing bauxite residue with a minor amount of additives at temperatures of 1200-1300 °C, followed by quenching, allowed the production of a reactive precursor that consisted of a mixture of amorphous (25 - 62 wt%) and inert, iron-rich crystalline phases. By adjusting the additions of CaO and SiO_2, the performance of alkali-activated mortars from these vitrified BRs can be optimised to reach compressive strengths of 110 MPa at 7 days and 130 MPa at 28 days with a low shrinkage of 1.5 mm/m within 180 days.

444 It was found that the amount of CaO added, determined to a great extent the 7 and 28 d compressive
445 strength. An increasing amount of CaO in the amorphous phase led to an increase in the bound water
446 content of the final binder, which is either stronger/denser with a less permeable pore structure. This
447 also had a positive effect on the dimensional changes during drying. Furthermore, this work also
448 suggests the importance of Al_2O_3 in increasing the 28 d compressive strength for these IPs. The
449 environmental performance of the material was evaluated with batch leaching tests and radionuclide
450 measurements. In both categories, the mortar performed well and, in terms of radioactivity, it can be
451 safely used in indoor applications.

452 This work identified an optimum chemistry and processing conditions concerning the mechanical and
453 environmental performance. In addition, the results show that the quality of the amorphous/glass
454 phase is more important than the quantity. In principle, all BRs produced from the Bayer process can
455 be transformed into a vitrified BR with the optimum bulk chemistry. The adjustments required for
456 different BRs and its real time implementation in an alumina plant is at the moment under
457 investigation.

458 ## 5 Acknowledgements

459 The research leading to these results has been performed within the REMOVAL project and received
460 funding from the European Community's Horizon 2020 Programme (H2020/2014-2020) under grant
461 agreement no. 776469. The authors would like to offer special thanks to Manuël Adams (2020 †) for
462 his help with density measurements. Sadly, he is no longer with us. Also a big thanks to Pieter L'hoëst
463 for his help and expertise regarding EPMA.

464

465

466

467

6 Appendix

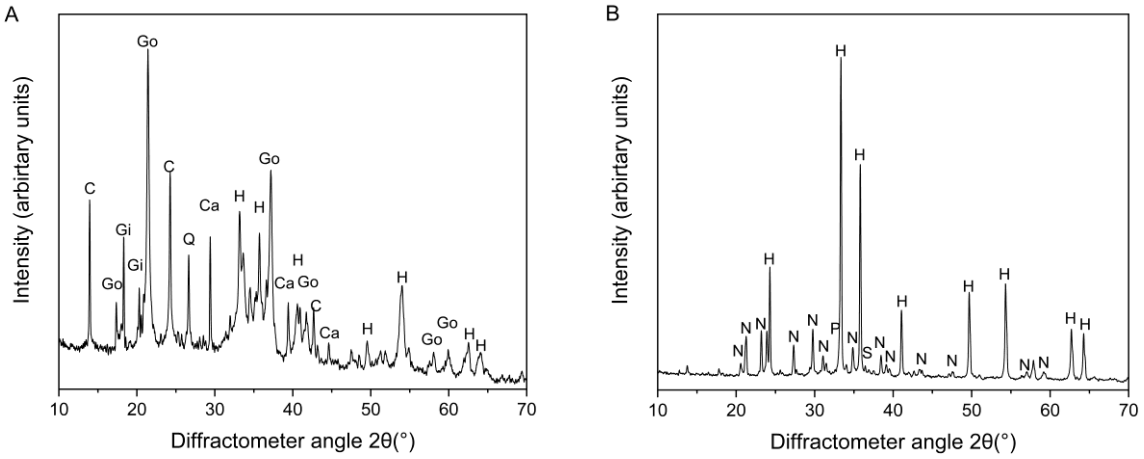

Figure A1:A) XRD of the raw BR dried at 105 °C: C: cancrinite, Go: goethite, Gi: gibbsite, Q: quartz, Ca: calcite, H: hematite. B) XRD of the used calcined BR at 950 °C. H: hematite; N: nepheline, P: perovskite and S: sodalite.

Table A1: Average composition of the identified sodium alumina silicate phases using EDX in wt% with standard deviation.

	Na_2O	Al_2O_3	SiO_2	CaO	TiO_2	FeO
Si0Ca0-1200	26.8 ± 1.1	38.9 ± 1.8	29.2 ± 1.4	1 ± 0.6	0.1 ± 0.2	4.1 ± 1.2
Si0Ca10-1200	30.2	47.5	19.3	0.9	-	2.1
Si10Ca0-1200	20.8 ± 0.1	34.5 ± 1	38.6 ± 2.1	2.3 ± 0.1	-	3.7 ± 3.0
Si5Ca5-1200	22.8 ± 0.2	37.2 ± 0	34.8 ± 0.5	0.9 ± 0.2	-	4.3 ± 0.6
Si10Ca10-1200	-	-	-	-	-	-
Si10Ca10-1300	-	-	-	-	-	-

Table A2: Average composition of the calcium alumina silicate phase (Gehlenite) in wt% with standard deviation.

	Na_2O	Al_2O_3	SiO_2	CaO	TiO_2	FeO
Si0Ca10-1200	0.7 ± 0.1	35.3 ± 0.4	20 ± 0.9	41.4 ± 0.3	0 ± 0	2.6 ± 0.7

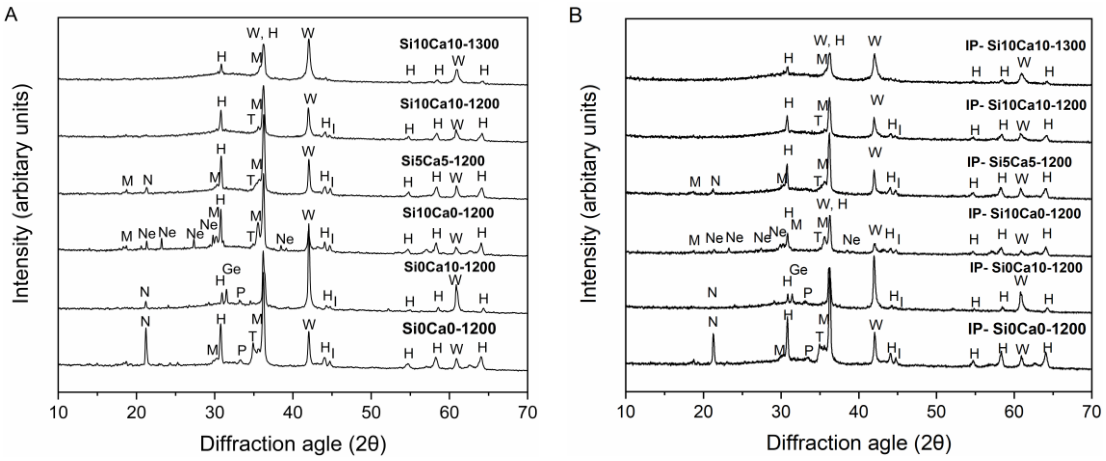

Figure A2: A) XRD of the VBR samples. H: hercynite, M: magnetite, W: wüstite, I: iron, T: titanomagnetite, Ne: sodium alumina silicate phase reflecting the chemistry and crystal structure of nepheline, N: sodium aluminosilicate phase with orthorhombic crystal structure, Ge: calcium alumina silicate phase identified as gehlenite. B) XRD of the IP paste samples after 28 days.

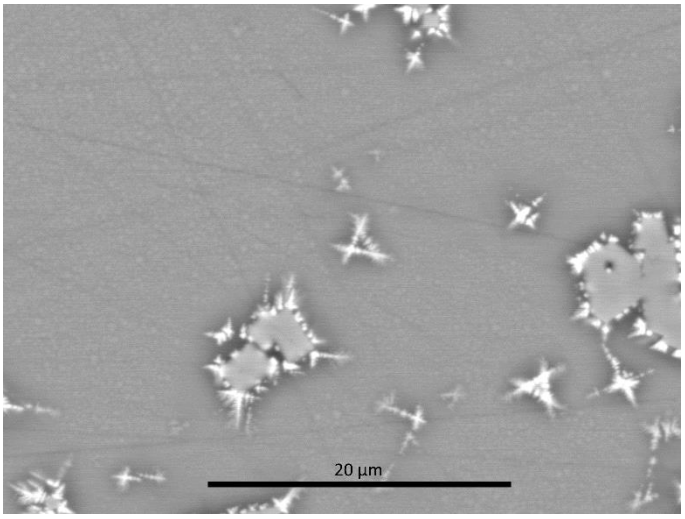

Figure A3: Appearance of crystals (cloudy) in the matrix with the amorphous phase in between.

7 References

[1] A.R. Hind, S.K. Bhargava, S.C. Grocott, The surface chemistry of Bayer process solids: A review, Colloids Surfaces A Physicochem. Eng. Asp. (1999). https://doi.org/10.1016/S0927-7757(98)00798-5.

[2] K. Evans, The history, challenges, and new developments in the management and use of bauxite residue, J. Sustain. Metall. 2 (2016) 316–331. https://doi.org/10.1007/s40831-016-0060-x.

[3] G. Bánvölgyi, Personal communication, (2020).

[4] P.J.M. Monteiro, S.A. Miller, A. Horvath, Towards sustainable concrete, Nat. Mater. 16 (2017) 698–699. https://doi.org/10.1038/nmat4930.

[5] J.L. Provis, S.A. Bernal, Geopolymers and Related Alkali-Activated Materials, Annu. Rev. Mater. Res. 44 (2014) 299–327. https://doi.org/10.1146/annurev-matsci-070813-113515.

[6] K. Komnitsas, D. Zaharaki, V. Perdikatsis, Effect of synthesis parameters on the compressive strength of low-calcium ferronickel slag inorganic polymers, J. Hazard. Mater. (2009). https://doi.org/10.1016/j.jhazmat.2008.04.055.

[7] S. Onisei, Y. Pontikes, T. Van Gerven, G.N. Angelopoulos, T. Velea, V. Predica, P. Moldovan, Synthesis of inorganic polymers using fly ash and primary lead slag, J. Hazard. Mater. 205–206 (2012) 101–110. https://doi.org/10.1016/j.jhazmat.2011.12.039.

[8] R.I. Iacobescu, V. Cappuyns, T. Geens, L. Kriskova, S. Onisei, P.T. Jones, Y. Pontikes, The influence of curing conditions on the mechanical properties and leaching of inorganic polymers made of fayalitic slag, Front. Chem. Sci. Eng. 11 (3) (2017) 317–327. https://doi.org/10.1007/s11705-017-1622-6.

[9] A. Peys, L. Arnout, H. Rahier, B. Blanpain, Y. Pontikes, V.A. Karel, Mix-design Parameters and Real-life Considerations in the Pursuit of Lower Environmental Impact Inorganic Polymers, Waste and Biomass Valorization. 9 (2018) 879–889. https://doi.org/10.1007/s12649-017-9877-1.

[10] J. Van De Sande, A. Peys, T. Hertel, H. Rahier, Y. Pontikes, Upcycling of non-ferrous metallurgy slags: Identifying the most reactive slag for inorganic polymer construction materials, Resour. Conserv. Recycl. 154 (2020) 104627. https://doi.org/10.1016/j.resconrec.2019.104627.

[11] A. Peys, E.C. White, D. Olds, H. Rahier, B. Blanpain, Y. Pontikes, Molecular structure of CaO-FeOx-SiO2 glassy slags and resultant inorganic polymer binders, J. Am. Ceram. Soc. 101 (2018) 5846–5857. https://doi.org/10.1063/1.1732055.

[12] S. Simon, G.J.G. Gluth, A. Peys, S. Onisei, D. Banerjee, Y. Pontikes, The fate of iron during the alkali-activation of synthetic (CaO-)FeO x -SiO 2 slags: An Fe K -edge XANES study, J. Am. Ceram. Soc. (2018) 1–12. https://doi.org/10.1111/jace.15354.

[13] T. Hertel, Y. Pontikes, Geopolymers, inorganic polymers, alkali-activated materials and hybrid binders from bauxite residue (red mud) – Putting things in perspective, J. Clean. Prod. 258 (2020) 120610. https://doi.org/10.1016/j.jclepro.2020.120610.

[14] D.D. Dimas, I.P. Giannopoulou, D. Panias, UTILIZATION OF ALUMINA RED MUD FOR SYNTHESIS OF INORGANIC POLYMERIC MATERIALS, Miner. Process. Extr. Metall. Rev. 30 (2009) 211–239. https://doi.org/10.1080/08827500802498199.

[15] P. Krivenko, O. Kovalchuk, A. Pasko, T. Croymans, M. Hult, G. Lutter, N. Vandevenne, S.

Schreurs, W. Schroeyers, Development of alkali activated cements and concrete mixture design with high volumes of red mud, Constr. Build. Mater. 151 (2017) 819–826. https://doi.org/10.1016/j.conbuildmat.2017.06.031.

[16] T. Hertel, B. Blanpain, Y. Pontikes, A proposal for a 100 % use of bauxite residue towards inorganic polymer mortar, J. Sustain. Metall. 2 (2016) 394–404. https://doi.org/10.1007/s40831-016-0080-6.

[17] X. Ke, S.A. Bernal, N. Ye, J.L. Provis, J. Yang, One-part geopolymers based on thermally treated red Mud/NaOH blends, J. Am. Ceram. Soc. 98 (2015) 5–11. https://doi.org/10.1111/jace.13231.

[18] N. Ye, J. Yang, S. Liang, Y. Hu, J. Hu, B. Xiao, Q. Huang, Synthesis and strength optimization of one-part geopolymer based on red mud, Constr. Build. Mater. 111 (2016) 317–325. https://doi.org/10.1016/j.conbuildmat.2016.02.099.

[19] T. Hertel, R.M. Novais, R. Murillo Alarcón, J.A. Labrincha, Y. Pontikes, Use of modified bauxite residue-based porous inorganic polymer monoliths as adsorbents of methylene blue, J. Clean. Prod. 227 (2019) 877–889. https://doi.org/10.1016/j.jclepro.2019.04.084.

[20] T. Hertel, A. Van den Bulck, B. Blanpain, Y. Pontikes, Correlating the amorphous phase structure of vitrified bauxite residue (red mud) to the initial reactivity in binder systems, Submitt. to Cem. Concr. Res. (2021).

[21] C.W. Bale, E. Bélisle, P. Chartrand, S.A. Decterov, G. Eriksson, K. Hack, I.H. Jung, Y.B. Kang, J. Melançon, A.D. Pelton, C. Robelin, S. Petersen, FactSage thermochemical software and databases - recent developments, Calphad Comput. Coupling Phase Diagrams Thermochem. 33 (2009) 295–311. https://doi.org/10.1016/j.calphad.2008.09.009.

[22] C. Siakati, A.P. Douvalis, P. Ziogas, A. Peys, Y. Pontikes, Impact of the solidification path of FeOx–SiO2 slags on the resultant inorganic polymers, J. Am. Ceram. Soc. 103 (2020) 2173–2184. https://doi.org/10.1111/jace.16869.

[23] EN 196-6, Methods of testing cement - Part 6: Determination of fineness, 2010.

[24] R. Snellings, L. Machiels, G. Mertens, J. Elsen, Rietveld Refinement strategy for Quantitative Phase analysis of Partially AMorphous zeolitized tuffaceous rocks, Geol. Belgica. 13 (2010) 183–196.

[25] EN 196-1, Methods of testing cement - Part 1: Determination of strength, 2016.

[26] EN 12457-4, Characterisation of waste — Leaching — Compliance test for leaching of granular waste materials and sludges, 2002.

[27] Council of the European Union, Council Decision establishing criteria and procedures for the acceptance of waste at landfills pursuant to Article 16 of and Annex II to Directive 1999/31/EC, Off. J. Eur. Communities. (2003) 27–49.

[28] K. Gijbels, H. Nguyen, P. Kinnunen, P. Samyn, W. Schroeyers, Y. Pontikes, S. Schreurs, M. Illikainen, Radiological and leaching assessment of an ettringite-based mortar from ladle slag and phosphogypsum, Cem. Concr. Res. 128 (2020) 105954. https://doi.org/10.1016/j.cemconres.2019.105954.

[29] Council Directive 2013/59/Euratom, Laying down basic safety standards for protection against the dangers arising from exposure to ionising radiation, and repealing, 2014.

[30] B. Mysen, P. Richet, Silicate glasses and melts, 2005.

[31] K.L. Aughenbaugh, T. Williamson, M.C.G. Juenger, Critical evaluation of strength prediction methods for alkali-activated fly ash, Mater. Struct. Constr. 48 (2014) 607–620. https://doi.org/10.1617/s11527-014-0496-z.

[32] R.I. Iacobescu, I. Annelies, L. Machiels, P.T. Jones, B. Blanpain, Y. Pontikes, Stabilisation and Microstructural Modification of Stainless Steel Converter Slag by Addition of an Alumina Rich By-Product, Waste Biomass Valorization. 5 (2014) 343–353. https://doi.org/10.1007/s12649-013-9287-y.

[33] R. Snellings, Surface chemistry of calcium aluminosilicate glasses, J. Am. Ceram. Soc. 98 (2015) 303–314. https://doi.org/10.1111/jace.13263.

[34] J.P. Hamilton, S.L. Brantley, C.G. Pantano, L.J. Criscenti, J.D. Kubicki, Dissolution of nepheline , jadeite and albite glasses : Toward better models for aluminosilicate dissolution, Geochim. Cosmochim. Acta. 65 (2001) 3683–3702.

[35] H. Maraghechi, F. Rajabipour, C.G. Pantano, W.D. Burgos, Effect of calcium on dissolution and precipitation reactions of amorphous silica at high alkalinity, Cem. Concr. Res. 87 (2016) 1–13. https://doi.org/10.1016/j.cemconres.2016.05.004.

[36] A.M. Rashad, A synopsis about the effect of nano-Al2O3, nano-Fe2O3, nano-Fe3O4 and nano-clay on some properties of cementitious materials - A short guide for Civil Engineer, Mater. Des. (2013). https://doi.org/10.1016/j.matdes.2013.05.035.

[37] G. Geng, R.J. Myers, J. Li, R. Maboudian, C. Carraro, D.A. Shapiro, P.J.M. Monteiro, Aluminum-induced dreierketten chain cross-links increase the mechanical properties of nanocrystalline calcium aluminosilicate hydrate, Sci. Rep. 7 (2017) 1–10. https://doi.org/10.1038/srep44032.

[38] E.I. Diaz, E.N. Allouche, S. Eklund, Factors affecting the suitability of fly ash as source material for geopolymers, Fuel. 89 (2010) 992–996. https://doi.org/10.1016/j.fuel.2009.09.012.

[39] P.T. Durdziński, R. Snellings, C.F. Dunant, M. Ben Haha, K.L. Scrivener, Fly ash as an assemblage of model Ca-Mg-Na-aluminosilicate glasses, Cem. Concr. Res. 78 (2015) 263–272. https://doi.org/10.1016/j.cemconres.2015.08.005.

[40] A. Schöler, F. Winnefeld, M. Ben Haha, B. Lothenbach, The effect of glass composition on the reactivity of synthetic glasses, J. Am. Ceram. Soc. 100 (2017) 2553–2567. https://doi.org/10.1111/jace.14759.

[41] P. Chindaprasirt, T. Phoo-ngernkham, S. Hanjitsuwan, S. Horpibulsuk, A. Poowancum, B. Injorhor, Effect of calcium-rich compounds on setting time and strength development of alkali-activated fly ash cured at ambient temperature, Case Stud. Constr. Mater. 9 (2018) e00198. https://doi.org/10.1016/j.cscm.2018.e00198.

[42] X. Yao, T. Yang, Z. Zhang, Compressive strength development and shrinkage of alkali-activated fly ash–slag blends associated with efflorescence, Mater. Struct. Constr. 49 (2016) 2907–2918. https://doi.org/10.1617/s11527-015-0694-3.

[43] G. Ascensão, G. Beersaerts, M. Marchi, M. Segata, F. Faleschini, Y. Pontikes, Shrinkage and Mitigation Strategies to Improve the Dimensional Stability of CaO-FeOx-Al2O3-SiO2 Inorganic Polymers, Mater. 12 (2019) 3679–3699. https://doi.org/10.1021/ja00897a054.

[44] C. Kuenzel, L.J. Vandeperre, S. Donatello, A.R. Boccaccini, C. Cheeseman, Ambient Temperature Drying Shrinkage and Cracking in, J. Am. Ceram. Soc. 3277 (2012) 3270–3277. https://doi.org/10.1111/j.1551-2916.2012.05380.x.

[45] Y.A. Villagrán-Zaccardi, H. Egüez-Alava, K. De Buysser, E. Gruyaert, N. De Belie, Calibrated

quantitative thermogravimetric analysis for the determination of portlandite and calcite content in hydrated cementitious systems, Mater. Struct. Constr. 50 (2017). https://doi.org/10.1617/s11527-017-1046-2.

[46] M. Giels, R.I. Iacobescu, V. Cappuyns, Y. Pontikes, J. Elsen, Understanding the leaching behavior of inorganic polymers made of iron rich slags, J. Clean. Prod. 238 (2019) 11. https://doi.org/10.1016/j.jclepro.2019.117736.

[47] B. Michalik, G. de With, W. Schroeyers, Measurement of radioactivity in building materials – Problems encountered caused by possible disequilibrium in natural decay series, Constr. Build. Mater. 168 (2018) 995–1002. https://doi.org/10.1016/j.conbuildmat.2018.02.044.

[48] C. Klauber, M. Gräfe, G. Power, Bauxite residue issues: II. options for residue utilization, Hydrometallurgy. 108 (2011) 11–32. https://doi.org/10.1016/j.hydromet.2011.02.007.

[49] P.J. Joyce, A. Björklund, Using Life Cycle Thinking to Assess the Sustainability Benefits of Complex Valorization Pathways for Bauxite Residue, J. Sustain. Metall. 5 (2019) 69–84. https://doi.org/10.1007/s40831-019-00209-x.

[50] C. Nuccetelli, Y. Pontikes, F. Leonardi, R. Trevisi, New perspectives and issues arising from the introduction of (NORM) residues in building materials: A critical assessment on the radiological behaviour, Constr. Build. Mater. 82 (2015) 323–331.

[51] W. Schroeyers, Z. Sas, G. Bator, R. Trevisi, C. Nuccetelli, F. Leonardi, S. Schreurs, T. Kovacs, The NORM4Building database, a tool for radiological assessment when using by-products in building materials, Constr. Build. Mater. 159 (2018) 755–767. https://doi.org/10.1016/j.conbuildmat.2017.11.037.

645